Available online at www.sciencedirect.com
ScienceDirect
Journal of Nuclear Materials 366 (2007) 58–69
journal of nuclear materials
www.elsevier.com/locate/jnucmat

Dislocation structures in 16MND5 pressure vessel steel strained in uniaxial tension at different temperatures from −196 °C up to 25 °C

C.F. Robertson [a,*], K. Obrtlik [b], B. Marini [a]

[a] Commissariat à l'Energie Atomique (Saclay), DEN/DMN/SRMA/LC2M, bât. 455, 91191 Gif-sur-Yvette, France
[b] Institute of Physics of Materials, Academy of Sciences of the Czech Republic, Zizkova 22, 616 62 Brno, Czech Republic

Received 26 June 2006; accepted 15 December 2006

Abstract

16MND5 ferritic steel specimens are strained in uniaxial tension at different temperatures, from −196 °C up to 25 °C. The TEM observations made after the tests reveal that strain localization takes place at the scale of lath blocks, where the individual laths undergo bending straining. Noticeably, the lath boundary dislocations represent an important fraction of the initial sources. Within the deformed laths, dislocations are homogeneously distributed at low plastic strain and gradually condense into high density structures, with increasing deformation. Dislocation condensation takes place in the form of cell walls or tilt boundary structures at $T \geqslant 0$ °C; in the form of sub-lath size clusters at $T \leqslant -90$ °C. Unlike in pure iron, screw dislocation motion in 16MND5 steel is characterized by very active cross-slip and subsequent formation of cross-kinks. It is believed that this self-locking effect contributes to strain hardening, in addition to dislocation accumulation at the lath boundaries.

---

1. Introduction

16MND5 ferritic steel is used to manufacture the pressure vessels of pressurized water nuclear reactors. The prevention of brittle fracture in these components is a fundamental issue in nuclear plant life management. Generally, brittle fracture in pressure vessel steels has a cleavage character. Most of the cleavage mechanisms described in the literature involve crystal plasticity associated with the generation, motion and interaction of dislocations [1]. For this reason, it is believed that toughness prediction and especially its temperature dependence could be better established, by using models accounting for dislocation based plasticity. In practice, brittle fracture takes place when the local stress state presents a sufficient tri-axiality, i.e. includes a high maximal principal stress [2,3].

In α-iron, it is known since many years that the behaviour of dislocations is temperature dependent. In the past, dislocation structures developing in uniaxial straining were studied extensively, both in single crystals and poly-crystals of pure iron [2,4]. The type of microstructures formed, either uniform

---

[*] Corresponding author. Tel.: +33 1 69 08 22 70; fax: +33 1 69 08 71 67.
E-mail address: christian.robertson@cea.fr (C.F. Robertson).

0022-3115/$ - see front matter © 2007 Elsevier B.V. All rights reserved.
doi:10.1016/j.jnucmat.2006.12.043

density structures or cell structures, was shown to depend on both the strain level and the test temperature [4]. In 16MND5 bainitic steel however, data on the evolution of the dislocation structures with temperature and plastic strain is missing. This material is made of very thin grains (laths) and therefore a significant effect of the internal interfaces on the dislocations arrangements can be expected. This work aims to document and analyse the various dislocation structures formed after tensile straining at different temperatures, representative of the whole ductile to brittle transition domain of the steel.

2. Experimental details

16MND5 steel (AISI denomination: A508CL3) pieces were first taken from a pressure vessel nozzle cut off. After forging, the heat treatment of the material was the following: twice austenization at 865/895 °C for 4 h 30 min and water quenched then, tempering at 630/645 °C for 7 h 30 min followed by stress relieving at 610 °C for 8 h. A complete characterization of the material under study was reported elsewhere [5], including tensile tests on notched specimens and fracture toughness tests on CT specimens.

The heat treatment results in a bainitic microstructure, made of blocks of parallel ferrite laths (see Fig. 1(a)). The typical individual lath is 10–25 × 10–25 μm large, whereas the individual lath thickness is 1–2 μm. In this paper, the direction parallel to the lath thickness is called the **C**-axis. The TEM micrographs taken on different foils from the same specimen are quite variable, depending on the micro-structural features contained within the foil. When the foil plane is parallel to the local **C**-axis, only the lath cross-sections are present and thus, visualized. In contrast, when the foil plane is perpendicular to the **C** axis, the foil cuts through either the lath bulk or the lath interface (see figure caption 1(b)), yielding very different images.

The chemical composition of the 16MND5 steel is given in Table 1. The tensile specimen geometry adopted in this study is cylindrical with threaded ends and a gauge diameter of 4 mm. The specimens were machined from pieces cut at one fourth of the vessel wall thickness. Fig. 2(a) shows the specimen dimensions. The specimen loading axis is parallel to the surface of the pressure vessel ring, along the vessel axial direction. The tensile tests were performed in an electro-hydraulic testing machine INSTRON at a rate of $5 \times 10^{-5}\ \mathrm{s}^{-1}$ up to the plastic strains of 2.5% and 8%, for the testing temperatures of $T = -196$ °C, -90 °C, 0 °C. One additional tensile test has been carried out at $T = 25$ °C in the same conditions as before, up to the plastic strain of 11%.

When the tensile tests are stopped at the completion of the selected plastic strains, the specimen is removed from the testing machine for observation in a TEM Philips CM-20 operating at 200 kV, using a double tilt holder. Thin foils were prepared using the standard double jet technique, from sections cut at an angle of 45° to the specimen axis. Special care

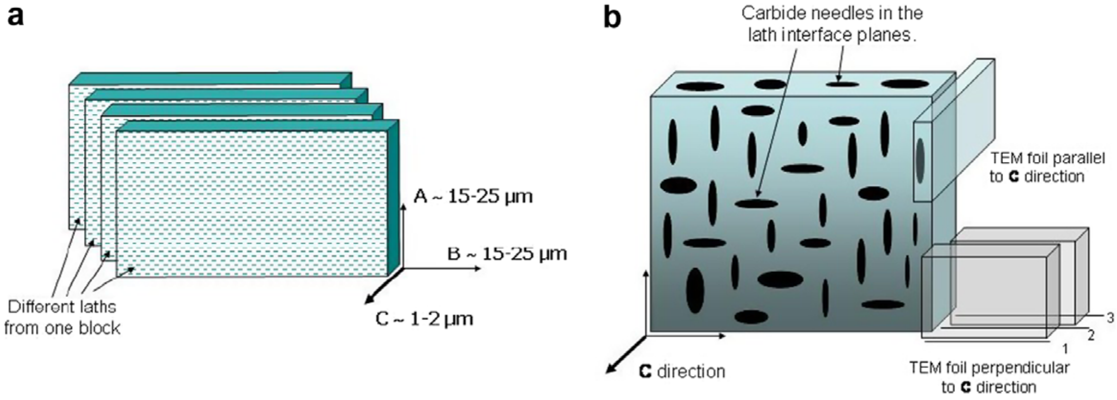

Fig. 1. Sketch of the lath block structure in bainite. (a) One block of laths is represented with the typical dimensions in directions **A**, **B** and **C**. The actual lath extremities in directions **A** and **B** are sharper than pictured. (b) Interpretation scheme for the TEM observations: when the foil plane is cut parallel to the averaged **C** direction in a lath block, only the lath cross sections are visible. When the foil plane is cut parallel to the **C** direction, the foil is either comprised between markers 2 and 3, or between markers 1 and 2, since the typical TEM foil thickness (100–200 nm) is about one tenth of the lath thickness. In the first case (markers 2–3), the whole lath plane **C** is visible. In the second case (markers 1–2), the whole lath boundary is visible, including all the inter-lath carbides.

Table 1
Composition of 16MND5 steel (wt%)

C	S	P	Mn	Si	Ni	Cr	Mo	V	Cu	Co	Al
0.16	0.008	0.005	1.38	0.24	0.70	0.17	0.50	0.005	0.06	0.01	0.020

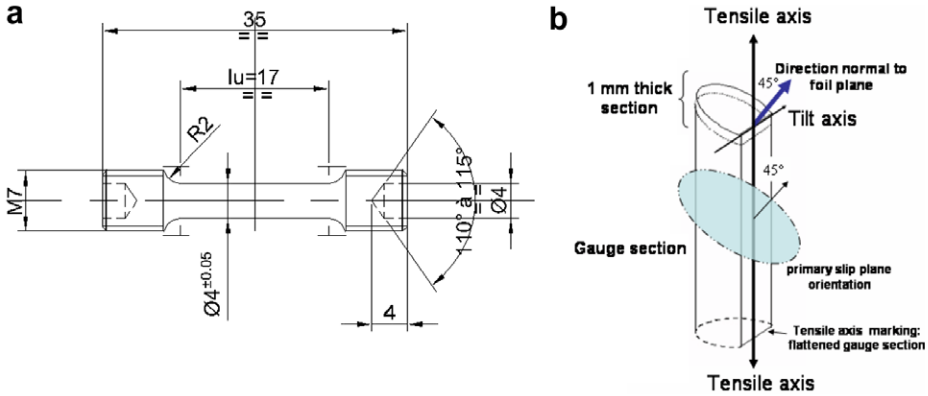

Fig. 2. Tensile specimen geometry. (a) Specimen dimensions, (b) sketch of the specimen markings made before to thin foil cutting. The initially circular gauge section is flattened along the longitudinal direction and then cut at 45° from the tensile loading axis, using spark machining. This way, the (1 mm thick) sections cut parallel to the new oblique section include a short, rectilinear portion. After thin foil preparation, this rectilinear portion is aligned with the tilt axis of the specimen holder. Hence, in the TEM coordinate system, the tensile axis is at the same time perpendicular to the specimen holder tilt axis and 45° away from the foil plane.

was taken to mark the tensile direction (see Fig. 2(b)) and so, the orientation of each lath relative to the loading axis could be determined using diffraction patterns or Kikuchi lines.

3. Results

3.1. Stress–strain curves

The experimental load–elongation curve was converted into a stress–strain curve, under the assumption of uniform elongation of the gauge length. Fig. 3 shows the stress–strain curve of the steel obtained at the test temperatures $T = -196$ °C, -90 °C and 0 °C. The stress–strain curve at $T = 25$ °C is not shown but is similar to the curve obtained at $T = 0$ °C. High yield point, yield drop and ductile straining zone characterize tensile testing at -196 °C, in agreement with the behaviour of other bcc metals [6–8]. At this temperature, a Luders plateau is obtained for plastic strains up to 3%, when uniform gauge section specimens are used. However, the plateau is suppressed when sharp notched specimens are used [5]. Hence, this phenomenon is ascribed to structural effects rather than to the (averaged) mobile dislocation density evolutions. In most of the tests, the plastic strain of 2.5% corresponds to the end of the plateau. This minimal test interruption level was selected (see Fig. 3) with a view to facilitate the analysis of subsequent TEM examinations (structural effects are indeed limitted past 2.5% plastic strain). Despite that precaution however, deformation along the specimen length is not uniform, regardless of the testing conditions (see Section 3.3). The yield stress sharply decreases from about 900 MPa down to 550 MPa, when the temperature increases from $T = -196$ °C to $T = -90$ °C. The yield stress change is comparatively smaller between $T = -90$ °C and $T = 0$ °C, i.e. from about 550 MPa

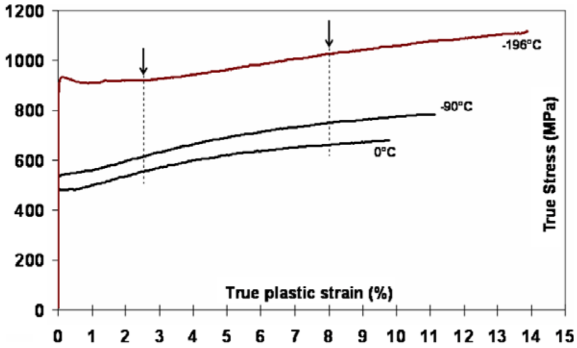

Fig. 3. Stress–strain curves of the steel at different temperatures. The arrow markers indicate the plastic strain of the interrupted tensile tests: 2.5% and 8%.

down to 450 MPa. The relative strain hardening rate change between $T = -196$ °C and $T = 0$ °C is slight, i.e. from about 2 GPa up to 2.5 GPa (at 2.5% plastic strain).

3.2. *Dislocation arrangements in the initial material condition*

The initial dislocation densities in the material (prior to straining) are in the range of $10^{13}\ \mathrm{m}^{-2}$ to $2 \times 10^{14}\ \mathrm{m}^{-2}$, depending on the individual laths. The dislocation densities are measured by summing up the total dislocation length located in $2\ \mu\mathrm{m} \times 2\ \mu\mathrm{m}$ representative TEM foil regions. The selected regions present sharp thickness fringes, when using 2 g imaging conditions. This way, the local foil thickness measurement is straightforward. The lath having the largest dislocation densities ($2 \times 10^{14}\ \mathrm{m}^{-2}$) comprise wall structures, likely formed during the prior heat treatment (see the arrow markers, in Fig. 4(a)). These structures are more frequent in the vicinity of lath or block boundaries. The laths showing less important dislocation densities ($10^{13}\ \mathrm{m}^{-2}$) comprise uniform dislocation distributions (see Fig. 4(b)). In TEM, lath boundaries usually produce a typical moiré-like fringe contrast. Using specific tilt angles however, the presence of regularly spaced screw dislocation arrays can be evidenced, in the lath interfaces (see Fig. 5). The average spacing between the interfacial dislocations is about 3–6 nm. These lines present specific Burgers vectors, obtained at the time of lath growth [9]. In lath boundaries having the proper orientation with respect to the foil plane (in TEM foils cut between markers 1–2, in Fig. 1(b)), carbides in the form of needles or globular particles are also visible, with a mean diameter of 0.1 µm. These particles partially cover the lath boundaries, with an area fraction 60–80%. The individual lath misorientations within a given lath block are nowhere larger than 5°. The original austenitic grain size was evaluated to be 50 µm. Sporadic, isolated particles up to 10 µm in size are observed as well.

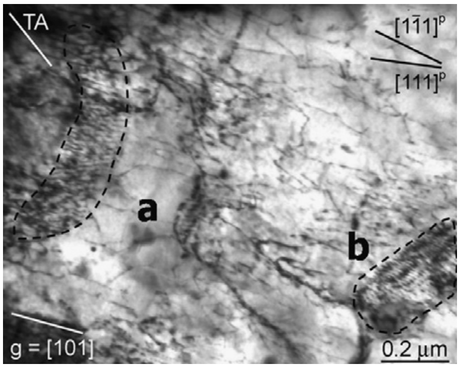

Fig. 5. Example of lath boundary dislocations viewed in sharp contrast conditions. The dislocations next to markers a and b have the screw type, with the [1 1 1] and [−1 1 1] Burgers vectors. The foil was cut perpendicular to the lath extremities, whereas the directions **A** or **B** are nearly parallel to the beam direction. The beam direction is [−3 2 0 3], $g = [1\,0\,1]$, the foil plane is close to (0 1 0). The label TA means the projection of the tensile axis in the image plane.

3.3. *Dislocation arrangements in deformed tensile specimens*

3.3.1. *Dislocation arrangements at $T = 25$ °C and 11% plastic strain*

In practice, the dislocation densities can vary from a bainitic lath to a lath. The volume fraction of the deformed laths is larger than 50%. The

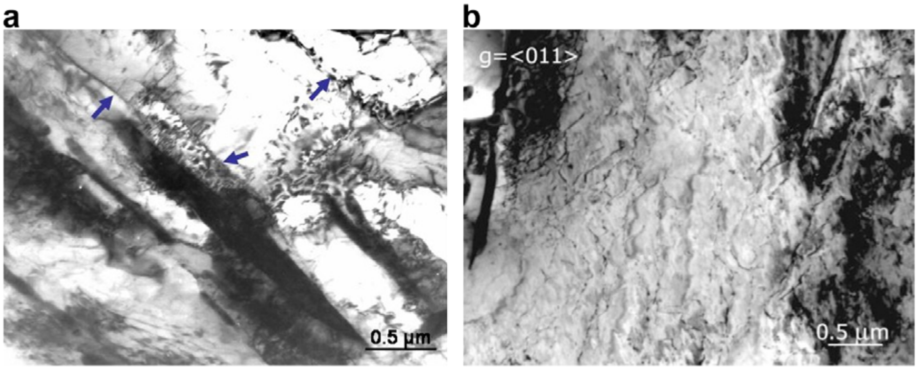

Fig. 4. Intra-lath dislocation structures before tensile testing. (a) A fraction of the laths contain dislocation wall nucleus probably formed during annealing (arrow markers). The average dislocation density in those laths is about $\rho = 2 \times 10^{14}\ \mathrm{m}^{-2}$. (b) Laths exhibiting a uniform dislocation density $\rho = 10^{13}\ \mathrm{m}^{-2}$. In micrographs (a) and (b), the lath **C**-axis is nearly parallel to the foil plane.

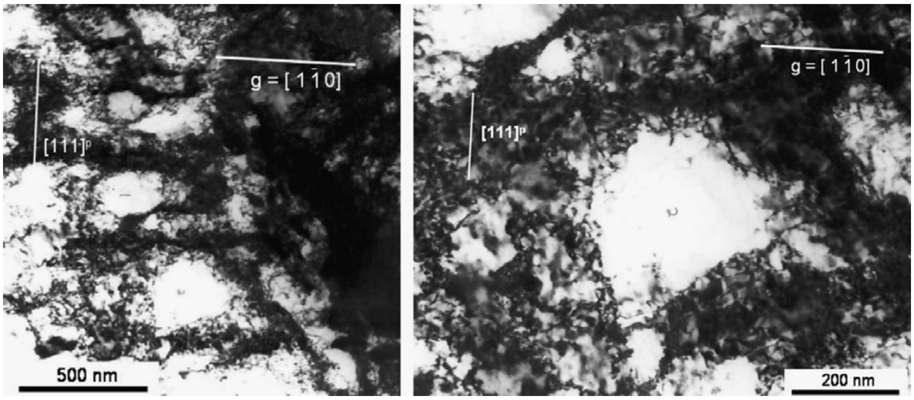

Fig. 6. Equiaxial dislocation cells formed at $T = 25$ °C after 11% plastic strain. The beam direction is close to [0 0 1], $g = [1\,-1\,0]$, the lath **C**-axis is more or less perpendicular to the foil plane. The label $[1\,1\,1]^{\mathrm{p}}$ means the projection of the [1 1 1] direction in the foil plane.

deformed laths are randomly scattered along the specimen length. In the following, attention was mainly paid to the deformed regions. The typical structures are equiaxial cell walls (see Fig. 6), with an average cell diameter of 100–200 nm. The corresponding surface slip markings are very wavy, which makes it difficult to unambiguously determine the slip plane orientations. Nevertheless, a fraction of the laths contain regular edge dislocations arrays (one dislocation every 7–10 nm, see Fig. 7(a)) instead of cell walls. These arrays are interpreted as tilt boundaries (see Section 4) and clearly involve dislocations from the (1 1 0)[1 1 1] slip system, as sketched in Fig. 7(b). A few laths exhibit uniform dislocation density distributions, as in Fig. 8(a). Comparison between Fig. 8(a) and (b) readily shows that the dislocations in lath-3 have the same Burgers vector ($b = a/2[1\text{–}11]$) as the dislocations in the lath-2/3 boundary, where small inter-lath carbide needles are also visible.

3.3.2. Dislocation arrangements at 0 °C

The volume fraction of the deformed laths increases with increasing amount of plastic deformation, attaining about 30% at 8% plastic strain. At low plastic strain (2.5%), the dislocation density is rather uniform, with numerous accompanying dislocation loop debris (see Fig. 9). When the plastic strain increases to 8%, the dislocations condense into either tilt boundaries or, in a few cases, into elongated cell arrangements (see Fig. 10(c)). In this material, elongated cells have been observed next to the rupture surface of CT specimens, after very large plastic strains due to ductile tearing [10]. Thus, the cell structures in Fig. 10(c) were possibly formed in the vicinity of important inclusion particles, located out of the plane where the TEM foil was cut. One specific example of tilt boundary structure is presented in Fig. 10(a), where the beam direction is perpendicular to primary the slip plane, unlike the usual viewing axis adopted in textbooks[1]. This structure is accompanied with a bending extinction contour, in evidence across the whole lath (foil cut along the lath **C**-axis)[2].

3.3.3. Dislocation arrangements at −90 °C

The volume fraction of the deformed laths decreases with decreasing temperature, attaining 15%, at 8% plastic strain. At 2.5% plastic strain, the deformed laths contain a uniform dislocation density distribution, with accompanying loop debris. The tilt boundaries as described in Sections 3.3.1 and 3.3.2 are no longer observed. Instead, the dislocation density becomes slightly heterogeneous and small dislocation clusters are formed, as shown in Fig. 11. The clusters tend to be aligned along the screw directions. With increasing plastic strain, the dislocation clusters increase in size (see Fig. 12), especially near the lath or prior γ grain boundaries.

3.3.4. Dislocation arrangements at −196 °C

The dislocation structures and surface slip markings obtained at $T = -196$ °C are described in more details in [11], where $\{1\,1\,0\}\langle 1\,1\,1\rangle$ active slip systems

---

[1] In textbooks, the viewing axis is usually parallel to the edge direction.

[2] The extinction contour visible in Fig. 10 is consistent with lattice rotation 5°–10°.

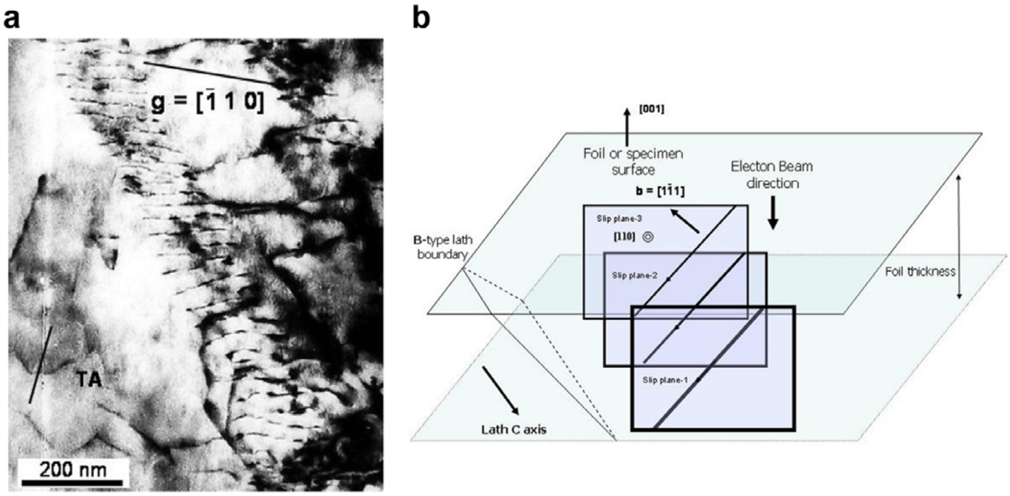

Fig. 7. Various examples of dislocation structures formed at $T = 25$ °C after 11% plastic strain. (a) Tilt boundary structure. (b) Sketch of the dislocation structure in micrograph-a. The beam direction is close to [0 0 1], $g = [-1\,1\,0]$ and the lath **C**-axis is nearly parallel to the foil plane.

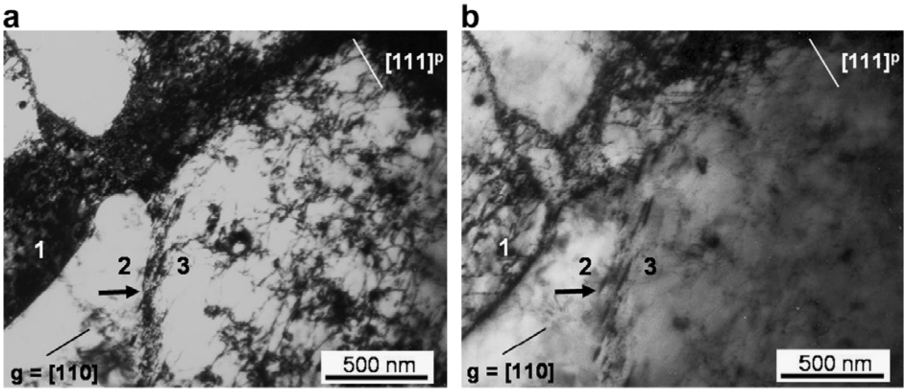

Fig. 8. Uniform density dislocation structure formed at $T = 25$ °C after 11% plastic strain. (a) The dislocations emitted in lath-3 and in lath-2/lath-3 boundary are in sharp contrast condition. (b) The dislocations in lath-3 and in lath-2/lath-3 boundary (arrow marker) are both out of contrast after a relative tilt of 2°, to micrograph a. Consequently, the dislocations in lath-3 have the same Burgers vector as the dislocations in lath-2/lath-3 boundary, where small inter-lath carbides are clearly visible. The beam direction is close to [0 0 1], $g = [1\,1\,0]$, the **C**-axis in lath-2 and lath-3 is more or less parallel to the foil plane.

are evidenced. The typical dislocation arrangement at 2.5% plastic strain is shown in Fig. 13: a uniform distribution of screw dislocations, with Burgers vector of the primary and secondary slip systems. When the plastic strain is increased to 8%, the dislocations have the same character as at low strain. Nevertheless, they are no longer homogeneously distributed within the laths and condensation in the form of clusters is clearly observed (see Fig. 14). In Fig. 13(b), accompanying dislocation loop debris are visible. Tilt boundaries are nowhere present in the material deformed at $T = -196$ °C, like at $T = -90$ °C.

4. Discussion

To the best of our knowledge, the active slip systems in 16MND5 steel have the $\{1\,1\,0\}\langle 1\,1\,1\rangle$ type, in the whole temperature range considered in this work. Strain localization in 16MND5 steel is nevertheless temperature dependent: the volume fraction of deformed laths increases from 10% at $T = -196$ °C up to about 30% at $T = 0$ °C, for the same amount of macroscopic plastic strain (8%). In the deformed laths of specimens strained at $T = 0$ °C and 25 °C, edge-type dislocation arrays are frequent (see Fig. 7). In the absence of disloca-

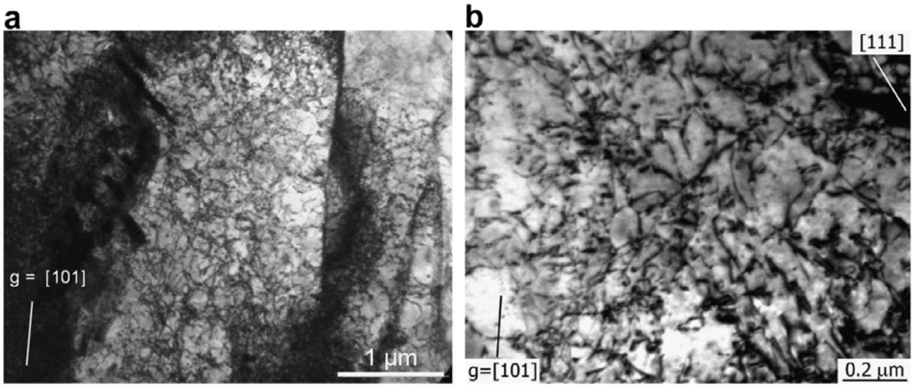

Fig. 9. Characteristic dislocation structures formed at $T = 0$ °C after 2.5% plastic strain. (a) Uniform density dislocation structures, (b) detail of micrograph-a, where screw and edge dislocations and dislocation loop debris are clearly visible. The beam direction is [−1 0 1], $g = [1\,0\,1]$, the lath **C**-axis is parallel to the foil plane.

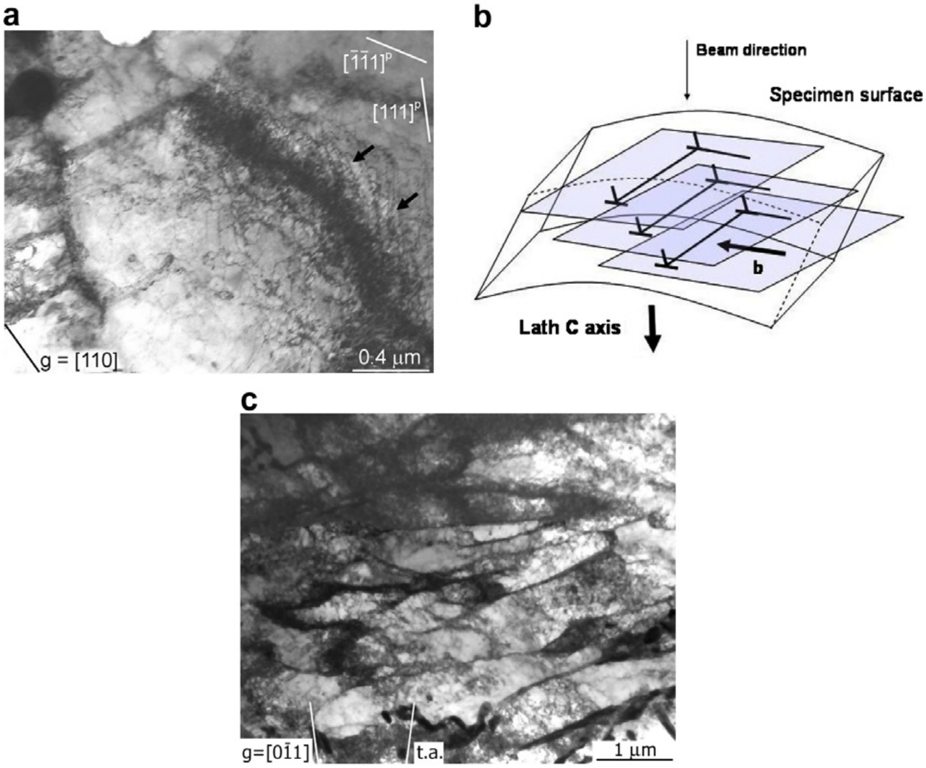

Fig. 10. Dislocation structures formed at $T = 0$ °C after 8% plastic strain. (a) Dislocation structure comprising at least two active slips systems, i.e. with $b = [1\,1\,1]$ and [−1–11]. The structure geometry is consistent with local bending moments parallel to the specimen surface, like the bending extinction contour visible across the whole lath. The beam direction is [−10 10 7] and $g = [1\,1\,0]$. (b) Sketch of the dislocation structure (next to the arrow markers) shown in micrograph-a, i.e. formed by dislocations with $b = [1\,1\,1]$. The whole structure shown in micrograph-a is more complex and probably includes a twist component, due to other active slip systems. (c) Example of elongated dislocation cells, with $g = [0–11]$. The lath **C**-axis is nearly perpendicular to the foil plane in micrographs-a and c.

tion climb, it is believed that these structures are inherited from the initial lath boundary dislocation structure; made of uniformly spaced, parallel dislocation lines (see Fig. 5). Direct evidence for interfacial dislocations acting as dislocation sources is presented in Fig. 8. When activated, the initial screw

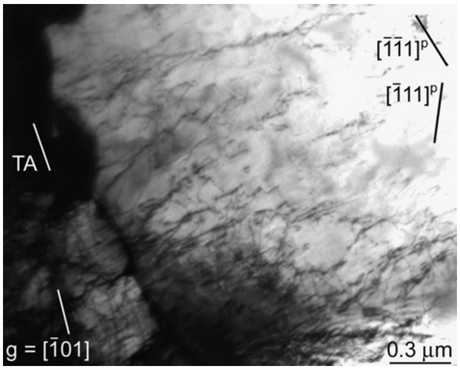

Fig. 11. Dislocation structures formed at $T = -90$ °C after 2.5% plastic strain. Small dislocation clusters are visible. This micrograph reveals the activity of lath boundary dislocation source, likely due to the complex, local stress state. The beam direction is [3 7 3], $g = [-1\,0\,1]$, the lath **C** axis is almost parallel to the foil plane.

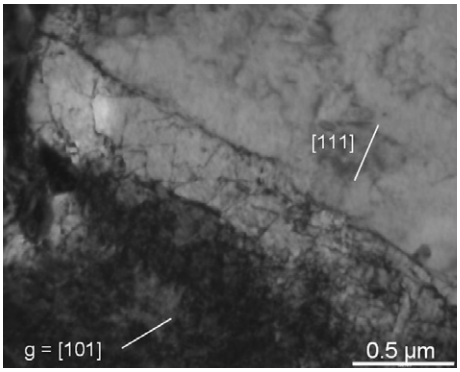

Fig. 12. Characteristic dislocations structures at $T = -90$ °C after 8% plastic strain. Large dislocation clusters. The beam direction is [−20 −3 20], the foil plane is close to (−1 0 1), $g = [1\,0\,1]$, the lath **C**-axis is nearly perpendicular to the foil plane.

segments (sources) move across the lath and leave edge segments in the crystal. Then, these edge segments are available to form edge-type arrays as sketched in Figs. 7(b) and 10(b). As a result, most of the edge-type dislocations tend to remain within the bulk of the laths and so, the majority of the dislocations crossing the lath interfaces are of the screw type. Since the mobile screw dislocations are in general parallel to the lath interfaces (see Section 3.2), clear surface markings are rather un-frequent, even after straining to 8% (see also [11], for details).

Dislocation structures as shown in Fig. 7 are also frequent in specimens undergoing macroscopic bending straining. For this reason, it is believed that bending also takes place here during tensile testing, albeit at the scale of the individual laths. In 16MND5 steel indeed, the tensile axis is generally not parallel to any of the main lath directions, either **A**, **B** or **C**. This, combined with the presence of disordered neighbouring lath blocks induces bending moments to which the small lath cross-section (in direction **C**) bears little resistance. That interpretation is supported by finite element method simulations, using meshing[3] representative of the 16MND5 steel lath block microstructure [12]. In these calculations, significant rotations are obtained inside the band-like, deformed regions[4]. The highly deformed bands are scattered across the simulation volume. They correspond to elements having specific orientations with respect to the loading direction and to the elements in neighbouring lath blocks. In general, large misorientations between contiguous lath blocks induce important, multi-axial rotations (or multi-axial bending straining). Based on these results, the regular edge-type dislocation arrays in Figs. 7 and 10 are interpreted as tilt boundary structures. This interpretation helps to establish the following lath deformation scheme. At low plastic strain, one tilt (or twist) array per loading axis is generated inside individual laths, provided dislocation sources are available in the appropriate, geometrically necessary slip system. For increasing deformation, screw dislocations from one slip system can add a twist component into a prior formed (and relatively immobile) tilt structure from a different slip system, giving rise to cell walls [13]. In 16MND5 steel at $T = 0$ °C and 25 °C, it is believed that the laths containing isolated tilt boundaries are moderately deformed, after single bending; whereas the laths containing cell walls come from more severely deformed lath blocks, undergoing multi-axial bending. It is also noted that the cell structures in deformed bainite are about 200–400 nm in size, whereas they are 1–2 µm large in pure iron poly-crystals with 100 µm grains, for the same plastic strain and test temperature [4]. Therefore, the cell size in 16MND5 steel scales with the lath size, in **A** or **B** directions (10–25 µm). This indicates that the carbide decorated lath boundaries

---

[3] The constitutive stress–strain behaviour of each Gauss point depends on the crystalline orientation attributed to each specific element, according to electron back-scattering diffraction (EBSD) data.

[4] Displacements are imposed to the appropriate boundary nodes. After loading beyond the yield point, the local rotations are computed by post-processing the node displacement data.

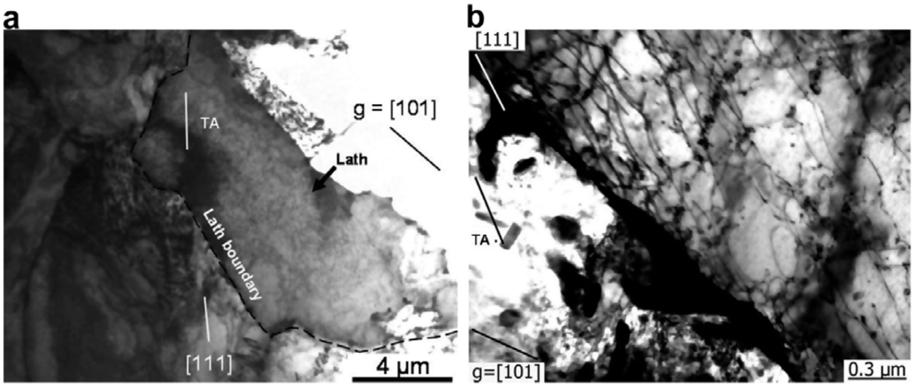

Fig. 13. Characteristic dislocation structure at $T = -196$ °C after 2.5% plastic strain. (a) Homogeneously distributed dislocations, (b) detail of micrograph-a, where series of aligned debris loops left by the [1 1 1] screw dislocations are clearly visible. The lath **C**-axis is almost perpendicular to the foil plane.

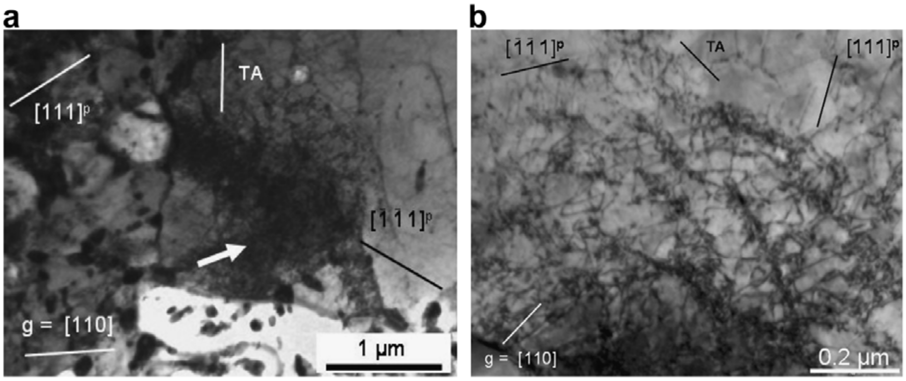

Fig. 14. Characteristic dislocation structures at $T = -196$ °C after 8% plastic strain. (a) Dislocation condensation into micron-sized clusters (arrow marker) is clearly visible, (b) detail of the cluster structure in micrograph-a. The beam direction is [−5 5 4], $g = [1\,1\,0]$, the lath **C**-axis is perpendicular to the foil plane.

can inhibit direct slip transmission from one lath to another[5], at least in the **A** or **B** directions (see Fig. 1).

For plastic strains larger than 2.5%, dislocations collect into high-density dislocation arrangements of different types, depending on the test temperature. This way, the tilt boundaries structures present in the deformed steel at $T \geqslant 0$ °C are absent at $T \geqslant -90$ °C. In contrast, the clusters found at $T \leqslant -90$ °C were not observed at $T \geqslant 0$ °C. In an attempt to explain this effect, it is interesting to note that the edge dislocations making up the tilt boundary structures (for $T \geqslant 0$ °C) are at least 200 nm long (see for example Fig. 7(a)). Conversely, the edge dislocations produced at lower temperature are in the form of loop debris or cross-kinks (see next paragraph) thus, are much smaller than 200 nm in size. In the present testing conditions thus, temperature fixes the length of the available edge dislocations. For $T \leqslant -90$ °C, the edge dislocations are possibly too short to form tilt boundary structures.

In bainitic steel, cross slip is quite active even at low plastic strain (2.5%) and for all test temperatures $T \leqslant 0$ °C, as attested by the numerous debris loops left on the dislocation wake, signature of double cross slip events (see for example Figs. 9(b), 13(b) and 14(b)). The intermediate stage in such a debris loop mechanism is the formation of ‘cross-kinks’ that directly result from collision of kinks formed in primary and cross slip planes and gliding in opposite directions [14]. The debris loops are emitted when proper kink pair nucleation events induce line reconnection in a single slip plane [15]. In principle, the cross-kinks are obstacles to

---

[5] In spite of the small inter-lath misorientations.

dislocation motion and can participate to mobile dislocation exhaustion, especially at low temperature, where dislocation pinning is weak and infrequent [11]. Screw dislocation motion associated with very active, random cross-slip and loop debris emission is sometimes called 'rough' [15]. Obviously, such screw dislocation motion is promoted by complex loading conditions,[6] due to multi-axial bending moments for example. One additional cause can be pointed out thanks to recent molecular dynamics (MD) simulations. In Ref. [16] indeed, it is showed that screw dislocations (loaded in single slip) in bcc iron undergoes random cross-slip, when the imposed stress exceeds a critical value. Incidentally, the activation energy in 16MND5 steel is significantly higher than in Fe[7] thus; the effective stress in 16MND5 steel is correspondingly larger than in Fe, for a fixed amount of plastic strain. This could explains in part why random cross-slip is clearly observed in bainitic steel and usually not in pure iron, neither in single nor in poly-crystals [4].

The strain hardening behaviour of the steel can be further analysed using an analytical model, assuming a uniform dislocation density.[8] The total dislocation density is first taken as the sum of the mobile dislocations ρ_{m} plus the immobile or stored dislocations ρ_{s}. Then, the following balance equations are proposed, based on information coming from in situ examinations in bcc crystals:

$$\dot{\rho}_{\mathrm{m}} = M\rho_{\mathrm{m}}V - A\rho_{\mathrm{m}}^2 V^2 - E\rho_{\mathrm{m}}V, \tag{1}$$

$$\dot{\rho}_{\mathrm{s}} = E\rho_{\mathrm{m}}V, \tag{2}$$

where V is the mobile dislocation velocity, M, A and E are constants characterizing dislocation multiplication, dislocation pair annihilation and mobile dislocation exhaustion, respectively. Dislocation multiplication and exhaustion involve single dislocations therefore; it is taken proportional to (ρV). Dislocation annihilation involves dislocation pairs thus; it is taken proportional to $(\rho V)^2$. The exhaustion kinetics $-E\rho_{\mathrm{m}}V$ in expression-(1) gives the immobile dislocation generation term $+E\rho_{\mathrm{m}}V$ in expression-(2). The evolution of the total dislocation density evolution is, by combining expressions (1) and (2)

$$\dot{\rho}_{\mathrm{t}} = \dot{\rho}_{\mathrm{m}} + \dot{\rho}_{\mathrm{s}} = M\rho_{\mathrm{m}}V - A\rho_{\mathrm{m}}^2V^2. \tag{3}$$

The mobile dislocation density at saturation is obtained from expression-(1) by taking $\dot{\rho}_{\mathrm{m}} = 0$, then

$$(M - E) - A\rho_{\mathrm{m}}V = 0. \tag{4}$$

Combining expression-(4) and the Orowan equation yields

$$\frac{\dot{\varepsilon}}{b} = \rho_{\mathrm{m}}V = \frac{M-E}{A}. \tag{5}$$

By combining expression-(3) and expression-(5), one obtains:

$$\dot{\rho}_{\mathrm{t}} = \frac{M-E}{A}\left[M - A\frac{M-E}{A}\right] = E\frac{M-E}{A} = \frac{E\dot{\varepsilon}}{b} \tag{6}$$

and finally, by integrating expression-(6)

$$\rho_{\mathrm{t}} = \rho_0 + \frac{E}{b}\dot{\varepsilon}t = \rho_0 + \frac{E}{b}\varepsilon. \tag{7}$$

At least two distinct contributions to the constant E are expected. The first contribution comes from the long range stress field due to the dislocations accumulating at the lath boundaries.[9] It is believed that dislocations accumulate at the lath boundaries thanks to the inter-lath carbide particles. In absence of particles, slip would probably be transmitted from one lath to the other, owing to the small inter-lath misorientations. In expression-(7), the hardening role of the carbides is thus implicitly accounted for. When random cross-slip takes place (at high effective stress), the second contribution comes from the self-locking effect due to the above-discussed cross-kinks. The need to account for the latter mechanism can be established (or dismissed) by computing the hardening due to the first contribution only. In that case, the stress increase is given by Taylor's expression, i.e. it is proportional to the square root of the total scalar dislocation density

$$\begin{aligned}\sigma &= \alpha\mu b\sqrt{\rho_{\mathrm{t}}} = \alpha\mu b\sqrt{\rho_0 + \frac{E}{b}\varepsilon}\\ &= \alpha\mu b\sqrt{\rho_0}\sqrt{1 + \frac{E}{\rho_0 b}\varepsilon},\end{aligned} \tag{8}$$

where α is a coefficient, characterizing the obstacle strength[10] and μ is the shear modulus. Differentiating equation-(8) with respect to ε yields

---

[6] Since a multi-axial loading generates stress components facilitating the activation of cross-slip.

[7] In Fe, the activation energy is $\Delta G = Ck_{\mathrm{B}}T$ with $C = 20$–25. In 16MND5 steel $C = 30$–40 (unpublished results).

[8] In 16MND5 steel, this assumption is valid at least up to 2.5% plastic strain.

[9] As mentioned above, the dislocation cell size scales with the lath size, in **A** or **B** directions.

[10] The strength of the lath boundaries, in that case.

$$\frac{\Delta\sigma}{\Delta\varepsilon}=\frac{\alpha\mu E}{2\sqrt{\rho_0}\sqrt{1+\frac{E}{\rho_0 b}\varepsilon}}=\frac{\alpha\mu E}{2\sqrt{\rho_t}}. \tag{9}$$

By comparing Figs. 9(b) and 13(b), it is readily established that quantity ρ_t is practically the same at $T=0$ °C and $T=-196$ °C (and $\varepsilon_p=2.5\%$). Qualitatively, expression-(9) explains the temperature independent strain hardening behaviour of 16MND5 steel (see Fig. 3), provided $\Delta(\alpha\mu E)/\Delta T\approx 0$. A quantitative validation of expression-(9) can be proposed by noting that the total screw dislocation density $\rho_{\text{screw}}\approx 2.5\times10^{13}\ \text{m}^{-2}$ in Fig. 13(b) represents about one tenth of the dislocation density in the lath boundaries.[11] Therefore, the initial number of screw dislocations is sufficient to accommodate the imposed straining and so, little multiplication actually takes place per individual (screw-type) source, in agreement with the lath deformation scheme sketched in Figs. 7(b) and 10(b). Hence, $\rho_0\approx\rho_{\text{screw}}=2.5\times10^{13}\ \text{m}^{-2}$ and by using $\alpha=0.3$, $\mu=74$ GPa, expression-(9) predicts the correct strain hardening (2 GPa, at $\varepsilon_p=2.5\%$) provided $E=6.7\times10^6\ \text{m}^{-1}$. To replace E in equation-(7) yields $\rho_t\approx2.2\times10^{15}\ \text{m}^{-2}$ at $\varepsilon_p=8\%$. This prediction is correct to the first order, by comparison with the (average) scalar dislocation densities in Fig. 14(b) (for example), i.e.$\rho_t\approx5\times10^{14}\ \text{m}^{-2}$. Better consistency can be achieved either by modifying expression-(8) or by using an ad-hoc α coefficient, characterizing the effective obstacle strength. Therefore, specific obstacle types or exhaustion mechanisms need to be accounted for in addition to the lath boundaries and their associated carbides, in order to achieve more accurate hardening predictions. Finally, it should be recalled that expression-(9) describes the averaged stress–strain behaviour related to homogenised dislocation density evolutions. Obviously, more development is needed in order to predict or to describe the hardening due to structural effects, like the Luders plateau obtained at low temperature (see Section 3.1).

5. Conclusions

From TEM examinations of the dislocation structures after tensile straining in 16MND5 bainitic steel between $T=-196$ °C and $T=25$ °C, the following conclusions are presented:

1. The screw dislocations located in the lath boundaries represent an important fraction of the initial sources, especially for $T\geqslant 0$ °C, where direct evidence has been obtained. To the best of our knowledge, the active slip systems have the $\{1\,1\,0\}\langle1\,1\,1\rangle$ type, in the whole temperature range considered in this work.
2. After the tests, strain localization takes place at the scale of lath block structures. At constant temperature, the volume fraction of the deformed zones increases with increasing plastic strain. At constant plastic strain, the volume fraction of the deformed zones increases with increasing temperature.
3. Even though the macroscopic loading is tensile, the individual laths tend to deform in bending, especially for $T\geqslant 0$ °C. This effect is believed to be related to specific lath block misorientations and to the comparatively small lath cross-section in direction **C**.
4. Within the deformed laths, the dislocations are distributed homogeneously at low plastic strain (2.5%) and gradually form denser structures, with increasing deformation (8%). Dislocation condensation takes place in the form of sub-lath size clusters at temperatures $T\leqslant -90$ °C, in the form of tilt boundaries and cell walls at temperatures $T\geqslant 0$ °C.
5. The cell structure sizes scale with the lath sizes in **A** or **B** type directions. This shows that the (carbide decorated) lath boundaries efficiently block direct slip transmission, from one lath to another. Dislocation accumulation at the lath boundaries is shown to be a first order contribution to the strain hardening behaviour.
6. Unlike in pure iron, screw dislocation motion in bainitic steel is characterized by very active, random cross-slip. This results in the formation of cross-kinks, a self-locking effect that most probably contributes to mobile dislocation exhaustion and therefore, to strain hardening. The important cross-slip activity is thought to be related to the relatively high effective stress acting in the steel.

Acknowledgements

This work was financially supported by the European project PERFECT and by a grant of the AS CR No. 1QS200410502. A part of the TEM observations were performed in the CEA-SRMP

---

[11] In the lath boundaries, $\rho_{\text{screw}}\approx2.2\times10^{14}\ \text{m}^{-2}$ using (25 µm × 25 µm × 1 µm) as a reference lath volume.

laboratory, with the kind support of Dr L. Boulanger. The analytical model presented in this paper (expressions (1)–(8)) was developed after an idea from Professor F. Louchet, whose contribution is gratefully acknowledged.

References

[1] A.G. Pineau, The Mechanical Behavior of Materials (ICM9); (2003), Paper No 71.

[2] D.J. Dingley, D. McLean, Acta Metall. 15 (1967) 885.

[3] S. Carassou, Doctoral thesis, Ecole des Mines de Paris, 1999.

[4] A.S. Keh, S. Weissmann, Electron Microscopy and Strength of Crystals, John Wiley, Interscience Publishers, New York, 1963, p. 231.

[5] S. Renevey, S. Carassou, B. Marini, C. Eripret, A. Pineau, J. Phys. IV 6 (1996) C6.

[6] J. Gil Sevillano, P. Van Houte, E. Aernoudt, Prog. Mater. Sci 25 (1980) 69.

[7] W.A. Spitzig, A.S. Keh, Acta Metall. 18 (1970) 611.

[8] W.A. Spitzig, A.S. Keh, Acta Metall. 18 (1970) 1021.

[9] H.K.D.H. Bhadeshia, second ed.Bainite in Steels, Transformations Microstructure and Properties, Cambridge University, 2001, p. 58.

[10] M. Karlik, I. Nedbal, J. Siegl, Mater. Sci. Eng. A 357 (2003) 423.

[11] K. Obrtlik, C. Robertson, B. Marini, J. Nucl. Mater. 342 (2005) 35.

[12] S. Sekfali, Doctoral thesis, Ecole Centrale de Paris, 2004.

[13] A. Seeger, Dislocations and Mechanical Properties of Crystals, John Wiley, New York, 1956.

[14] F. Louchet, B. Viguier, Phil. Mag. A 80 (2000) 765.

[15] J. Marian, W. Cai, V. Bulatov, Nature Mat. 3 (2004) 158.

[16] J. Chaussidon, D. Rodney, M. Fivel, Acta Mater. 54 (2006) 3407.